





Article

Modulation of Extracellular Matrix Composition and Chronic Inflammation with Pirfenidone Promotes Scar Reduction in Retinal Wound Repair

Laura Jahnke ^{1,2} , Virginie Perrenoud ¹, Souska Zandi ^{1,2}, Yuebing Li ^{1,2,3} , Federica Maria Conedera ^{1,4}  and Volker Enzmann ^{1,2,*} 

¹ Department of Ophthalmology, Bern University Hospital, University of Bern, 3010 Bern, Switzerland
² Department of BioMedical Research, University of Bern, 3008 Bern, Switzerland
³ Graduate School for Cellular and Biomedical Sciences, University of Bern, 3012 Bern, Switzerland
⁴ Department of Oncology, Microbiology and Immunology, University of Fribourg, 1700 Fribourg, Switzerland
* Correspondence: volker.enzmann@insel.ch; Tel.: +41-31-63-28-935

Abstract: Wound repair in the retina is a complex mechanism, and a deeper understanding of it is necessary for the development of effective treatments to slow down or even prevent degenerative processes leading to photoreceptor loss. In this study, we harnessed a laser-induced retinal degeneration model (532-nm laser photocoagulation with 300 µm spot size, 60 ms duration and 60 mV pulse), enabling a profound molecular elucidation and a comprehensive, prolonged observation of the wound healing sequence in a murine laser-induced degeneration model (C57BL/6J mice, 6–12 weeks) until day 49 post-laser. Our observations included the expression of specific extracellular matrix proteins and myofibroblast activity, along with an analysis of gene expression related to extracellular matrix and adhesion molecules through RNA measurements. Furthermore, the administration of pirfenidone (10 mg/kg via drinking water), an anti-inflammatory and anti-fibrotic compound, was used to modulate scar formation after laser treatment. Our data revealed upregulated collagen expression in late regenerative phases and sustained inflammation in the damaged tissue. Notably, treatment with pirfenidone was found to mitigate scar tissue formation, effectively downregulating collagen production and diminishing the presence of inflammatory markers. However, it did not lead to the regeneration of the photoreceptor layer.

Keywords: retina degeneration; wound repair; extracellular matrix; pirfenidone; fibrosis; inflammation; collagen



Citation: Jahnke, L.; Perrenoud, V.; Zandi, S.; Li, Y.; Conedera, F.M.; Enzmann, V. Modulation of Extracellular Matrix Composition and Chronic Inflammation with Pirfenidone Promotes Scar Reduction in Retinal Wound Repair. *Cells* **2024**, *13*, 164. <https://doi.org/10.3390/cells13020164>

Academic Editor: Girish Kumar Srivastava

Received: 12 December 2023

Revised: 11 January 2024

Accepted: 13 January 2024

Published: 16 January 2024



Copyright: © 2024 by the authors. Licensee MDPI, Basel, Switzerland. This article is an open access article distributed under the terms and conditions of the Creative Commons Attribution (CC BY) license (<https://creativecommons.org/licenses/by/4.0/>).

1. Introduction

Retinal fibrosis, which is the final phase of photoreceptor loss in retinal diseases such as age-related macular degeneration (AMD), includes the formation of degenerated tissue in the eye as a result of inflammatory responses and wound healing. The wound healing process is typically segmented into four distinct phases: hemostasis, inflammation, proliferation, and maturation. Fibrosis is a pathological condition characterized by the excessive accumulation of fibrous connective tissue, primarily composed of collagen. This process is a response to chronic inflammation, injury, or other underlying disorders and can lead to impaired tissue function and structural alterations. A fibrotic scar is formed by new extracellular matrix (ECM) hindering repair and resulting in vision loss [1,2]. In AMD, alteration of Bruch's membrane and chronic inflammation may lead to photoreceptor loss [3]. Numerous publications have established a connection between increased cytokine expression and progression of AMD [4–7]. Furthermore, local inflammation resulting from the buildup of cellular debris has been found to trigger drusen formation in AMD patients across all stages [8]. IL-1β has been shown to cause neurodegenerative damage, particularly in tissue with long-term exposure [9,10]. Tumor necrosis factor-α (TNF-α), among

others, has also been associated with the pathogenesis of AMD, and increased expression of this factor was found in a laser-induced choroidal neovascularization (CNV) model in mice [11]. Re-inflammation during the wound healing process leads to an inhibition of regeneration as new healthy tissue is damaged and cytokines have a profound modulatory effect on the regenerative activity of endogenous stem cells and progenitor cells [12]. As a result of chronic inflammation, the axons of neurons in the affected area continue to lose their ability to interact with other surrounding neurons and thus lose their functionality to process visual information to the brain [13].

Therefore, we aim to inhibit fibrosis and inflammation during the proliferative stage of wound healing by studying the influence of the non-peptide synthetic molecule pirfenidone (PFD) on retinal degeneration after laser-induced damage in the outer nuclear layer (ONL). PFD thus blocks transforming growth factor-beta (TGF- β). TGF- β is a multifunctional factor in fibrotic remodeling, capable of triggering myofibroblast transition, activating Smad signaling, and promoting the production of ECM [14]. Especially in the retina, transforming growth factor β (TGF- β) signaling demonstrates pleiotropic effects on various types of retinal cells, contributing to a wide array of functions, including the maintenance of retinal neuronal differentiation and viability, as well as the regulation of retinal vessel development and structural integrity [15]. PFD was approved in 2011 by the European Medicines Agency (EMA) and in 2014 by the U.S. Food and Drug Administration (Esbriet®) for the treatment of fibrotic diseases such as idiopathic pulmonary fibrosis in adults. Idiopathic pulmonary fibrosis is a chronic fibrotic and inflammatory lung disease characterized by release of pro-inflammatory cytokines, such as TNF- α and IL-1 β . Although the exact mechanism of action is not fully understood, the activity of connective tissue growth factor (CTGF), platelet-derived growth factor (PDGF), α -smooth muscle actin (α -SMA), and TGF- β is inhibited in the lung, as is the production of TNF- α , which plays an important role in inflammation [16,17]. It has also demonstrated interactions with a range of additional molecules known to play a role in fibrotic diseases. Thus, either direct (inhibition of IL-1 β , IL-6, IL-12p40, IL-13, IL-18 and increase of IL-10 secretion) or indirect (inhibition of TGF- β 1-induced over-expression of collagen type I and heat shock protein 47) actions are observed [18]. PFD also reduces fibroblast proliferation and the formation of fibrosis-associated proteins, such as collagen and fibronectin [17,19]. In ophthalmology, animal investigations suggest that PFD may have antifibrotic therapeutic potential for proliferative vitreoretinopathy (PVR) and could offer a promising approach to treating corneal haze [20–22]. Furthermore, in other experimental mouse models focused on choroidal neovascularization (CNV), it was shown that treatment with PFD leads to the inhibition of the fibrosis markers TGF- β 2, Smad2/3 and α -SMA [14,23]. PFD treatment offers also a promising avenue for addressing other eye pathologies involving inflammatory cytokines and pro-fibrotic growth factors [24].

In this study, the laser-induced retinal degeneration model led to photoreceptor loss with minimal rupture of Bruch's membrane followed by ECM formation and consequently scar formation in a focal area. After laser photocoagulation, we studied gene and protein levels of ECM proteins in the damaged retina. Furthermore, we investigated the impact of inhibiting inflammation and development of fibrosis with PFD on the formation of the ECM during retinal scar formation.

2. Materials and Methods

2.1. Laser-Induced Retinal Damage

All animal experiments followed the recommendations in the ARRIVE guidelines. Adult C57BL/6J mice (6–12 weeks, both sexes; Charles River Germany, Sulzfeld, Germany) were kept under standard conditions in individually ventilated cages (IVC) in a temperature-controlled animal facility with a 12-h light/dark cycle. They were fed standard laboratory chow and water ad libitum.

The mice were anesthetized with 1 mg/kg medetomidine (Domitor, 1 mg/mL; Provect AG, Lyssach, Switzerland) and 80 mg/kg ketamine (Ketalar, 50 mg/mL; Parke-Davis,

Zurich, Switzerland). The pupils were dilated with 2.5% phenylephrine and 0.5% tropicamide (ISPI, Bern, Switzerland). Hydroxypropyl methylcellulose (Methocel 2%; OmniVision AG, Neuhausen, Switzerland) was applied to keep the eyes hydrated. To induce retinal damage in the ONL without Bruch's membrane rupture, the eyes were lasered using a 300 µm spot size, a 60 ms duration, and 60 mV pulses of an 532-nm laser photocoagulation (Visulas 532s laser workstation with slit lamp; Carl Zeiss Meditec AG, Jena, Germany). Eight laser spots were centered with 2–3 disk diameters from the optic nerve, using a coverslip to allow for viewing of the posterior pole of the eye. Lesions in which bubbles, a criterion for Bruch's membrane rupture, were identified during the laser process were excluded from the study.

2.2. Pharmacological Treatment

Pirfenidone (PFD; 10 mg/kg; Catalog No. S2907, Selleck Chemicals, Houston, TX, USA) was administered via drinking water. To protect drug stability, the water bottles were shielded from light. The control animals received an equal amount of water under the same conditions. For monitoring, the animals were weighed three times per week. Water consumption was measured daily, and the water was changed on a daily basis. The PFD treatments started on day 14 post-laser injury until samples were collected (day 21, day 35, and day 42 post-laser). Additionally, to investigate the influence of retinal recovery, we terminated the PFD treatment on day 35 post-laser injury and harvested the retina 7 days later on day 42 post-laser. This sequence is defined as “D42 PFD D35” throughout the manuscript.

2.3. Histology

Paraffin-embedded sections (5 µm) of mouse eyes were deparaffinized and rehydrated with a graded series of xylol and alcohol. The sections were stained for 5 min with hematoxylin (Sigma, St. Louis, MO, USA) and 1 min with eosin (Roth, Karlsruhe, Germany) and then mounted with Eukitt® (Medite Service AG, Dietikon, Switzerland).

2.4. Immunohistochemistry

For immunostaining (IHC), deparaffinized samples were blocked at room temperature in blocking solution containing 3% normal goat serum (Agilent Technologies, Santa Clara, CA, USA), 0.5% casein (Sigma), and 0.05% Triton X-100 (Sigma) in Tris buffered saline (TBS) for 30 min. Primary antibodies (Abs) were added and incubated at 4 °C overnight; these were either Abs against gliosis-specific markers or ECM-relevant proteins, as summarized in Table 1. After incubation, sections were washed for 20 min and stained at room temperature with the respective secondary Abs (1:500; Alexa Fluor® 488 & 594 Abcam, Cambridge, UK) and 4',6-Diamidino-2-phenylindole (DAPI; Sigma) to counterstain nuclei for identification for 3 h. Images were acquired using a Nikon Eclipse 80i microscope (Nikon, Tokyo, Japan) at 20× magnification and processed using Image J 1.51n (Fiji-win64, NIH, Bethesda, MD, USA).

Table 1. Primary antibodies used for immunostaining (IHC) and Western blot (WB) analysis.

Antibody	Species	Type	Dilution	Company	Catalog. No.
αSMA	Rabbit	monoclonal	1:200 (IHC) 1:1000 (WB)	Novus Biologicals, Centennial, CO, USA	NBP2-67436
GS	Rabbit	monoclonal	1:200 (IHC)	Abcam, Cambridge, UK	ab16802
Isolectin GS-IB4	<i>Griffonia simplicifolia</i>	-	1:500 (IHC)	ThermoFisher Scientific, Reinach, Switzerland	I21412
GFAP	Mouse	monoclonal	1:1000 (IHC) 1:1000 (WB)	Novus Biologicals	NBP1-05197
Collagen 1	Rabbit	polyclonal	1:200 (IHC) 1:1000 (WB)	Novus Biologicals	NB600-408
Collagen 3	Rabbit	polyclonal	1:200 (IHC)	Novus Biologicals	NB600-594
Collagen 4	Rabbit	polyclonal	1:200 (IHC) 1:1000 (WB)	Novus Biologicals	PA1-28534
Collagen 5	Rabbit	polyclonal	1:200 (IHC)	Novus Biologicals	NBP1-68938

Table 1. Cont.

Antibody	Species	Type	Dilution	Company	Catalog. No.
Fibronectin	Rabbit	polyclonal	1:200 (IHC) 1:1000 (WB)	Novus Biologicals	NBP1-91258
GAPDH	Mouse	monoclonal	1:1000 (WB)	Novus Biologicals	NB300-221
IL-1 β	Rabbit	polyclonal	1:200 (IHC)	Abcam	ab9722
Versican	Rabbit	monoclonal	1:200 (WB)	Novus Biologicals	NBP2-75706

To determine the number of cells in the ganglion cell layer (GCL), the inner nuclear layer (INL), and the ONL, manual counting was performed within the lasered area in the hematoxylin and eosin (H&E) images. The size of the counted area corresponded to a retinal section 100 μ m in length.

2.5. Western Blot Analysis

To obtain tissue, the eyes were enucleated immediately after optical coherence tomography (OCT) imaging. The retinas were microsurgically isolated from the choroid-retinal pigment epithelium (RPE) complex, and two were combined in 100 μ L of lysis buffer (Table 2). There, they were supplemented with a protease inhibitor cocktail (cOmplete™ Mini; Merck, Darmstadt, Germany) and phosphatase inhibitors cocktail (P2850; Sigma) and homogenized (Precellys® 24 tissue homogenizer; Bertin Technologies S.A.S, Montigny-le-Bretonneux, France). The lysate was centrifuged (12,000 rpm, 15 min, 4 °C), and the supernatant was collected. Each sample containing 30 μ g of total protein, as quantified using the Bradford assay (ThermoFisher Scientific, Reinach, Switzerland), was separated via SDS-PAGE and electroblotted onto nitrocellulose membranes (Trans-Blot® Turbo™ Transfer System; Bio-Rad Laboratories, Cressier, Switzerland). To block nonspecific binding, the membranes were washed with milk Intercept™ (TBS) Blocking Buffer (LI-COR, Lincoln, NE, USA) and subsequently incubated at 4 °C overnight, followed by incubation for 3 h with a donkey anti-rabbit IgG polyclonal antibody (IRDye® 800CW) or donkey anti-mouse IgG polyclonal antibody (IRDye® 680RD), respectively. The signals were visualized using infrared laser (Li-Core Odyssey; LI-COR). Quantification was performed using Fiji-win64 (Image J; NIH).

Table 2. Lysis buffer ingredients.

Ingredients	Concentration
Tris-HCl (pH 7.5)	20 mM
NaCl	150 mM
EDTA	5 mM
Na-Pyrophosphate	5 mM
NaH ₂ PO ₄ (pH 7.6)	20 mM
Na- β -glycerophosphate	3 mM
NaF	10 mM

2.6. RNA Extraction and RT-qPCR

Total RNA from the retinas, including negative controls (uninjured retinas without drug treatment from age-matched siblings), was extracted at different time points (days 21, 35, and 42 days post-laser) after PFD treatment using the TRIzol™ (Thermo Fisher Scientific) according to the manufacturer's instructions. Three independent samples from two pooled retinas were used for each condition. The cDNA was reverse-transcribed using iScript cDNA Synthesis Kit (Bio-Rad) according to the manufacturer's instructions and quantified using a NANODROP 1000 spectrophotometer (Thermo Fisher Scientific). The primer sets are summarized in Table 3. RT-PCR was performed in a 20 μ L reaction containing cDNA specific primers with iTaq™ Universal SYBR Green Supermix (Bio-Rad) using the CFX Connect™ Real-Time PCR Detection System (Bio-Rad). The thermocycling conditions were as follows: 98 °C for 3 min, followed by 40 cycles at 98 °C for 15 s, 58 °C for 15 s, and 72 °C

for 15 s. The relative abundance of transcripts was normalized according to the relative abundance of the reference gene glyceraldehyde-3-phosphate-dehydrogenase (*GAPDH*). Gene expression was measured according to the change in threshold ($\Delta\Delta CT$). Expression data were presented as mean \pm SD calculated against the negative control samples, and expression in the control samples was set to 1.

Table 3. Primer Pairs for RT-qPCR.

Gene	Forward 5'-3'	Reverse 5'-3'	Annealing Temp.
<i>IL-1β</i>	GCC CAT CCT CTG TGA CTC AT	AGG CCA CAG GTA TTT TGT CG	58 °C
<i>GAPDH</i>	TGC ACC ACC AAC TGC TTA GC	GGC ATG GAC TGT GGT CAT GAG	58 °C

2.7. RT2 Profiler PCR Array

A SYBR green-based quantitative real-time RT2 qPCR array was used to profile genes involved in ECM composition as well as adhesion molecule deposition via cell–cell and cell–matrix interactions according to the manufacturer’s instructions (PAMM-013Z; QIAGEN, Hilden, Germany). The 96-well RT2 profile plate contained primers for 84 genes of interest (Table 4), five housekeeping genes, and three negative control wells. Also included are control elements for data normalization, genomic DNA contamination detection, RNA sample quality and general PCR performance. RNA extraction was performed as described previously. Briefly, 111 μ L cDNA was added to the master mix, and then 25 μ L was pipetted into each well. Real-time qPCR was performed on the Bio-Rad CFX 96 (Bio-Rad) using the following cycles: 1 cycle at 95 °C for 10 min, 40 cycles at 95 °C for 15 s and 60 °C for 1 min. A dissociation curve was performed at the end of the program to ensure the amplification of a single product. The results were normalized against the housekeeping gene and analyzed on an EXCEL-based spreadsheet (available on the QIAGEN website: <https://dataanalysis.qiagen.com/>). Ct values above 35 were deemed negative, and the normalized expression levels of lasered retinas were evaluated relative to non-lasered controls using the $2^{-\Delta\Delta Ct}$ method. A difference > 0.5 or < 0.5 indicated up- or downregulation, respectively.

Table 4. Summary of genes detected in the RT2 ECM and adhesion molecule kit.

Cell Adhesion Molecules	Transmembrane Receptors	<i>Cd44</i> , <i>Cdh1</i> (E-cadherin), <i>Cdh2</i> (N-cadherin), <i>Cdh3</i> , <i>Cdh4</i> , <i>Entpd1</i> , <i>Icam1</i> , <i>Itga2</i> , <i>Itga3</i> , <i>Itga4</i> (Cd49d), <i>Itga5</i> , <i>Itgae</i> , <i>Itgal</i> , <i>Itgam</i> , <i>Itgav</i> , <i>Itgb1</i> , <i>Itgb2</i> , <i>Itgb3</i> , <i>Itgb4</i> , <i>Mmp14</i> , <i>Mmp15</i> , <i>Ncam1</i> , <i>Ncam2</i> , <i>Pecam1</i> , <i>Sele</i> , <i>Sell</i> (Lecam-1), <i>Selp</i> , <i>Sgce</i> , <i>Syt1</i> , <i>Vcam1</i>
	Cell–Cell Adhesion	<i>Cdh1</i> (E-cadherin), <i>Icam1</i> , <i>Vcam1</i>
	Cell–Extracellular Matrix (ECM) Adhesion	<i>Ccn2</i> , <i>Itga2</i> , <i>Itga3</i> , <i>Itga4</i> (Cd49d), <i>Itga5</i> , <i>Itgae</i> , <i>Itgal</i> , <i>Itgam</i> , <i>Itgav</i> , <i>Itgax</i> , <i>Itgb1</i> , <i>Itgb2</i> , <i>Itgb3</i> , <i>Itgb4</i> , <i>Spp1</i>
	Other Cell Adhesion Molecules	<i>Cntn1</i> , <i>Col5a1</i> , <i>Col6a1</i> , <i>Ctnna1</i> , <i>Ctnna2</i> , <i>Ctnnb1</i> , <i>Emilin1</i> , <i>Fn1</i> , <i>Hapln1</i> , <i>Lama1</i> , <i>Lama2</i> , <i>Lama3</i> , <i>Lamb2</i> , <i>Lamb3</i> , <i>Lamc1</i> , <i>Postn</i> , <i>Tgfb1</i> , <i>Thbs1</i> (TSP-1), <i>Thbs2</i> , <i>Thbs3</i> , <i>Vcan</i> , <i>Vtn</i>
Extracellular Matrix (ECM) Molecules	Basement Membrane Constituents	<i>Col4a1</i> , <i>Col4a2</i> , <i>Col4a3</i> , <i>Entpd1</i> , <i>Itgb4</i> , <i>Lama1</i> , <i>Lama2</i> , <i>Lama3</i> , <i>Lamb2</i> , <i>Lamb3</i> , <i>Lamc1</i> , <i>Sparc</i> , <i>Timp1</i> , <i>Timp2</i> , <i>Timp3</i>
	Collagens and Extracellular Matrix (ECM) Structural Constituents	<i>Col1a1</i> , <i>Col2a1</i> , <i>Col3a1</i> , <i>Col4a1</i> , <i>Col4a2</i> , <i>Col4a3</i> , <i>Col5a1</i> , <i>Col6a1</i> , <i>Hapln1</i> , <i>Lama1</i>
	ECM Proteases	<i>Adamts1</i> , <i>Adamts2</i> , <i>Adamts5</i> , <i>Adamts8</i> , <i>Mmp10</i> , <i>Mmp11</i> , <i>Mmp12</i> , <i>Mmp13</i> , <i>Mmp14</i> , <i>Mmp15</i> , <i>Mmp1a</i> , <i>Mmp2</i> , <i>Mmp3</i> , <i>Mmp7</i> , <i>Mmp8</i> , <i>Mmp9</i>
	ECM Protease Inhibitors	<i>Col4a3</i> , <i>Timp1</i> , <i>Timp2</i> , <i>Timp3</i>
	Other ECM Molecules	<i>Ccn2</i> , <i>Ecm1</i> , <i>Emilin1</i> , <i>Fbln1</i> , <i>Fn1</i> , <i>Hc</i> , <i>Postn</i> , <i>Spock1</i> , <i>Spp1</i> , <i>Tgfb1</i> , <i>Thbs1</i> (TSP-1), <i>Tnc</i> , <i>Vcan</i>

2.8. Statistical Analysis

Values were presented as mean \pm SD. Normal distribution of the data and statistical differences (Student's *t*-test for two groups or one-way ANOVA with Bonferroni post hoc test for multiple comparison) were analyzed using GraphPad Prism 9 (GraphPad Software, Boston, MA, USA). Statistically significant differences are denoted by * with a probability value (*p*) of <0.05 , ** with $p < 0.01$, and highly significant differences by *** with $p < 0.001$ and **** with $p < 0.0001$.

3. Results

3.1. Extracellular Matrix and Fibrosis Development in Laser-Damaged Retina over Time

In order to quantify the laser-induced damage in the ONL, the mouse fundus was imaged using infrared scanning (IR), OCT b-scan images were recorded and H&E overview staining was performed at various time points, which revealed increased damage to the ONL with scarring over time (Figure 1A). Live images were taken every week from 12 h post-injury to day 49 to visualize wound healing. Quantification of the lesion area using OCT measurements of 60 lesions of 12 eyes from six mice showed a consistent reduction in lesion size until day 14. Afterwards, no significant reduction could be detected between day 14 and day 49 (Figure 1B). However, a significant difference was only documented when comparing day 1 and day 5 following laser induction. Furthermore, day 5 compared with day 49 showed a substantial reduction in lesion size. However, hyperintensity in OCT was stronger with time, indicating fibrosis.

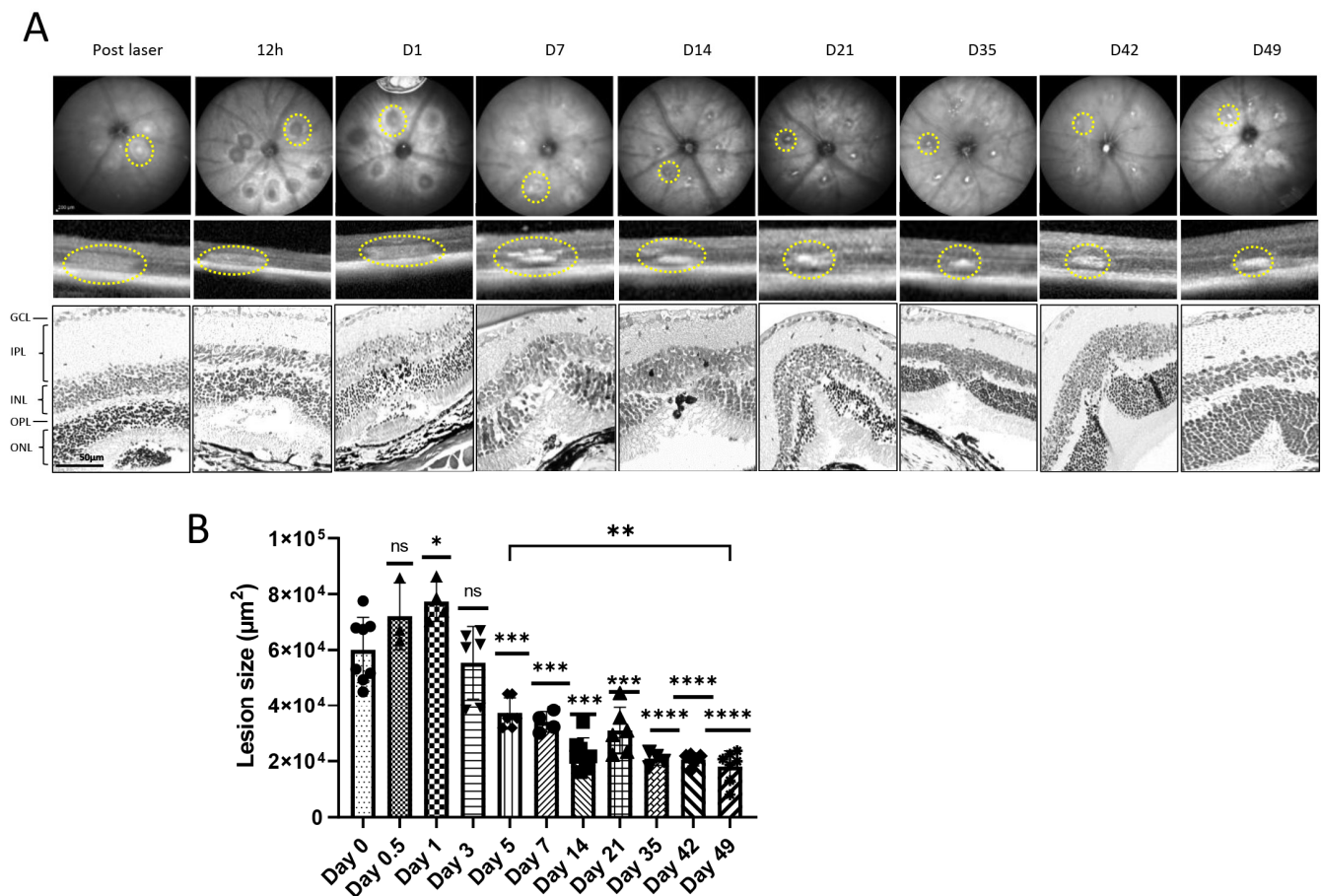


Figure 1. Fundus images of mouse retinas after photo coagulation with segmentation of OCT and representative retinal sections stained with H&E. (A) Fundus photographs were taken using infrared scanning (IR) (top) (scale bar is 200 μm) and SD-OCT (middle) at 12 h post-laser, as well as days 1,

7, 14, 21, 35, 42, and 49 post-laser. H&E (**bottom**) shows time-dependent formation of retinal scar with photoreceptor loss (yellow circle). (**B**) Quantification of the lesion area on all designated time points ($n = 60$ lesions of 10 eyes of 6 mice per time point). The significance was analyzed with one-way ANOVA with Bonferroni multiple comparisons test for $p = 0.05$ *, $p = 0.01$ **, $p = 0.0001$ ***, $p < 0.0001$ ****, ns = not significant.

To limit new vessel growth, the laser settings were modified to inflict soft tissue damage, and isolectin B4 was stained on day 7 post-laser to confirm absence of CNV at the earliest measured time point (Supplementary Figure S1).

High expression of fibronectin was detectable on days 1, 7, and 14 post-laser; decreased afterwards with its lowest expression on day 21; and then peaked on day 35 post-laser (white outlined areas in Figure 2). Moreover, fibronectin was found mainly in a scaffold in the RPE layer below the injury 12 h post-treatment. The expression of fibronectin was then found in all retinal layers at later time points from day 1 until day 49, but was detected in the RPE layer again on day 49 (Figure 2A,B). On day 35 post-laser, it was not present in the entire retina any more, with the expression restricted to the damaged area only on day 49. Western blot data also indicated a pattern of fibronectin protein expression across the entire retina with slight decrease until day 21 post-damage and a subsequent, more obvious decrease after day 35 (Figure 2C,D).

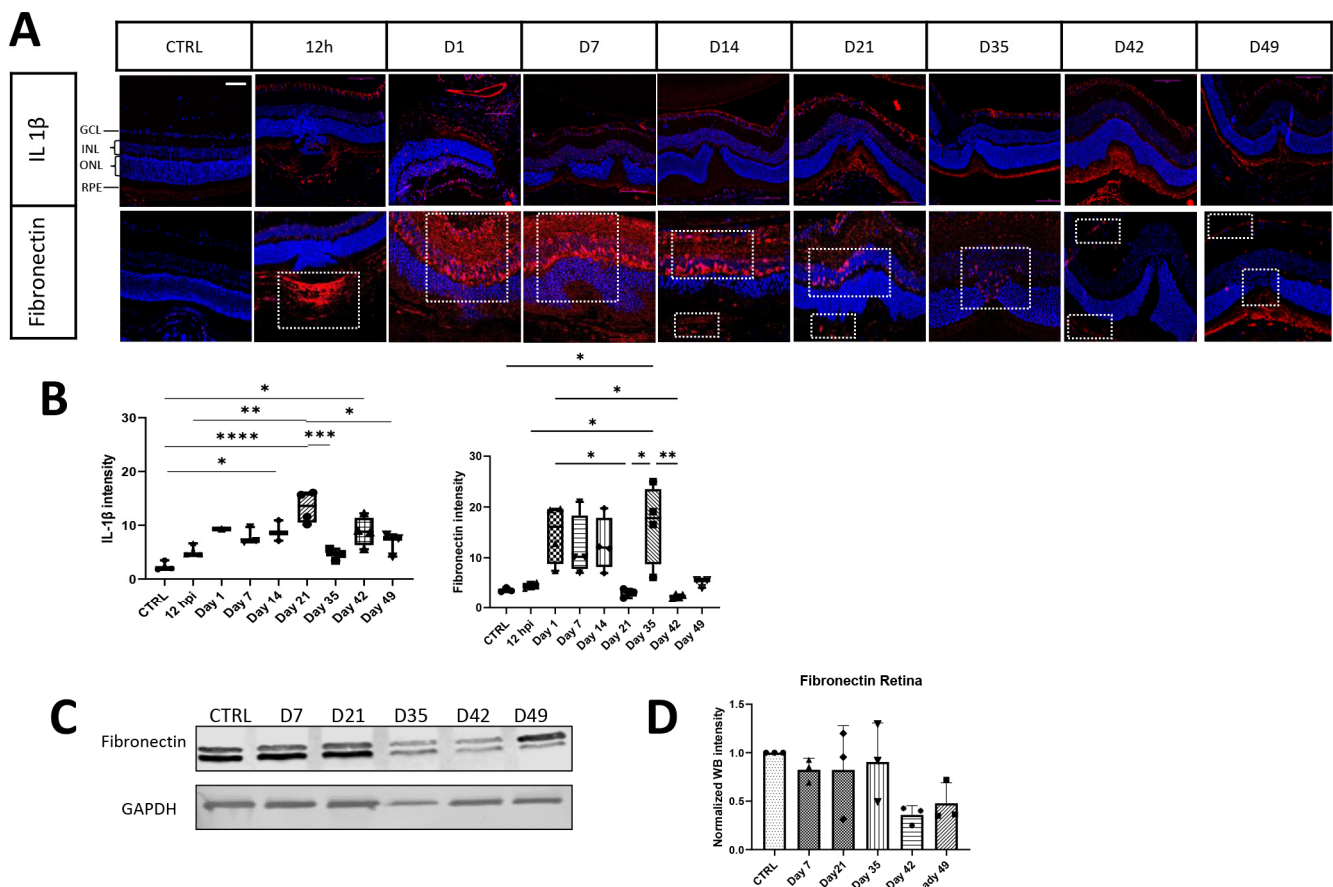


Figure 2. Time dependent expression of ECM markers. (**A**) Representative retinal section of control (CTRL) and lasered retinas on selected time points stained with specific antibodies against IL-1 β and fibronectin (red; white outlined) shown as merged images with DAPI staining (blue). Scale bar is 50 μ m. In (**B**), fluorescence intensity is shown in addition to the staining for every antibody. (**C,D**) Western blot analysis of fibronectin. Relative protein quantification has revealed a significant effect. Values are indicated as mean \pm SD. One-way ANOVA with Bonferroni multiple comparison test and * = $p < 0.05$, ** = $p < 0.01$, *** = $p < 0.001$, **** $p < 0.0001$, $n = 3$ /group. Scale bar: 50 μ m.

Additionally, the fibrotic response in the retina showed IL-1 β expression over time starting from day 1 until the last time point investigated (Figure 2A). Thus, IL-1 β expression reached its maximum on day 21 with a second wave of inflammation on day 42 post-laser (Figure 2B). Interestingly, IL-1 β and fibronectin increased similarly at the beginning of fibrosis (Days 1–14) but are expressed in the opposite way in the late phase (Days 21–49). This depicts the proliferation phase of non-pathological wound healing progressing as acute inflammation resolves.

Immunostaining showed that the signal intensity of the activated myofibroblast marker α SMA peaked on day 21, was reduced on day 35, and slightly increased again at day 42 post-laser (Figure 3A,B). In contrast, different collagens present in scar tissue as fiber-forming collagens 1, 3 and 5, as well as the non-fiber-forming collagen 4, increased later than α SMA detection, from 21 days until 49 days post-laser (Figure 3A,C). Collagen 1 reached a maximum on day 49, similar to collagen 5, whereas collagen types 3 and 4 showed their expression maximum on days 21 and 35 post-laser, respectively (Figure 3B,D). Apart from collagens, the multifunctional proteoglycan protein versican demonstrated a significant increase in expression in the retina, with the highest levels observed on day 40 post-damage, as detected through Western blot analysis (Figure 3C,D).

3.2. Extracellular Matrix-Related Genes Show Strong Dynamics during Tissue Replacement

To analyze ECM-involved genes, we used the RT² ProfilerTM PCR Array Mouse Extracellular Matrix & Adhesion Molecules array to profile 84 related genes (Supplementary Table S1) simultaneously for 5 selected data collection points (CTRL, day 7, day 21, day 35, and day 49). Beta2-microglobulin (B2m) was selected as the optimal internal control for the candidate genes provided in the PCR array using the Gene Globe program offered by QIAGEN.

3.2.1. General Comparison

Among the 84 genes studied, the majority (70 genes) were expressed at higher levels compared to the CTRL samples on day 49 post-laser, whereas 73 genes were expressed at lower levels compared to CTRL samples on day 21 post-laser (Figure 4). Of these genes, only five (*Col4a3*, *Fbln1*, *Itgal*, *Icam1*, and *Vcan*) showed statistically significant overexpression between the CTRL samples and day 49, the latest time point investigated ($n = 3$, $p > 0.05$). Additionally, *Vcan* showed a significant downregulation at day 21 ($n = 3$, $p > 0.05$; Supplementary Table S1). At day 7, four genes (*Cdh3*, *Icam1*, *Sell*, *Vcan*) showed significant different expression compared to the CTRL samples, while five genes (*Col3a1*, *Col4a1*, *Col4a3*, *Fbln1*, *Vcan*) did so on day 35 ($n = 3$, $p > 0.05$).

3.2.2. Extracellular Matrix Components

Twenty-six genes included in the array (*Col1a1*, *Col2a1*, *Col3a1*, *Col4a1*, *Col4a2*, *Col4a3*, *Col5a1*, *Col6a1*, *Ecm1*, *Emilin1*, *Fbln1*, *Fn1*, *Hapln1*, *Lama1*, *Lama2*, *Lama3*, *Lamb2*, *Lamb3*, *Lamc1*, *Sparc*, *Spock1*, *Spp1*, *Syt1*, *Tnc*, *Can*, *Vtn*) were clustered as a separate group of ECM matrix proteins (Figure 5A,B; Supplementary Table S1). Considering all time points, *Vcan* was significantly upregulated on days 35 and 49 ($n = 3$, $p > 0.05$). Furthermore, all collagen genes were significantly downregulated on day 21 ($n = 3$, $p \leq 0.05$). Versican and fibulin 1 (*Fbln1*) were the only two genes that were substantially upregulated at this time point ($n = 3$, $p \leq 0.05$). In comparison, 18 genes showed a trend towards upregulation (*Col4a3*, *Fbln1*, and *Vcan* significantly so) on day 49 ($n = 3$, $p > 0.05$). At this time point, only *Col2a1* was downregulated ($p = 0.176$). On day 35, *Col4a3* and *Fbln1* were significantly upregulated ($n = 3$, $p > 0.05$).

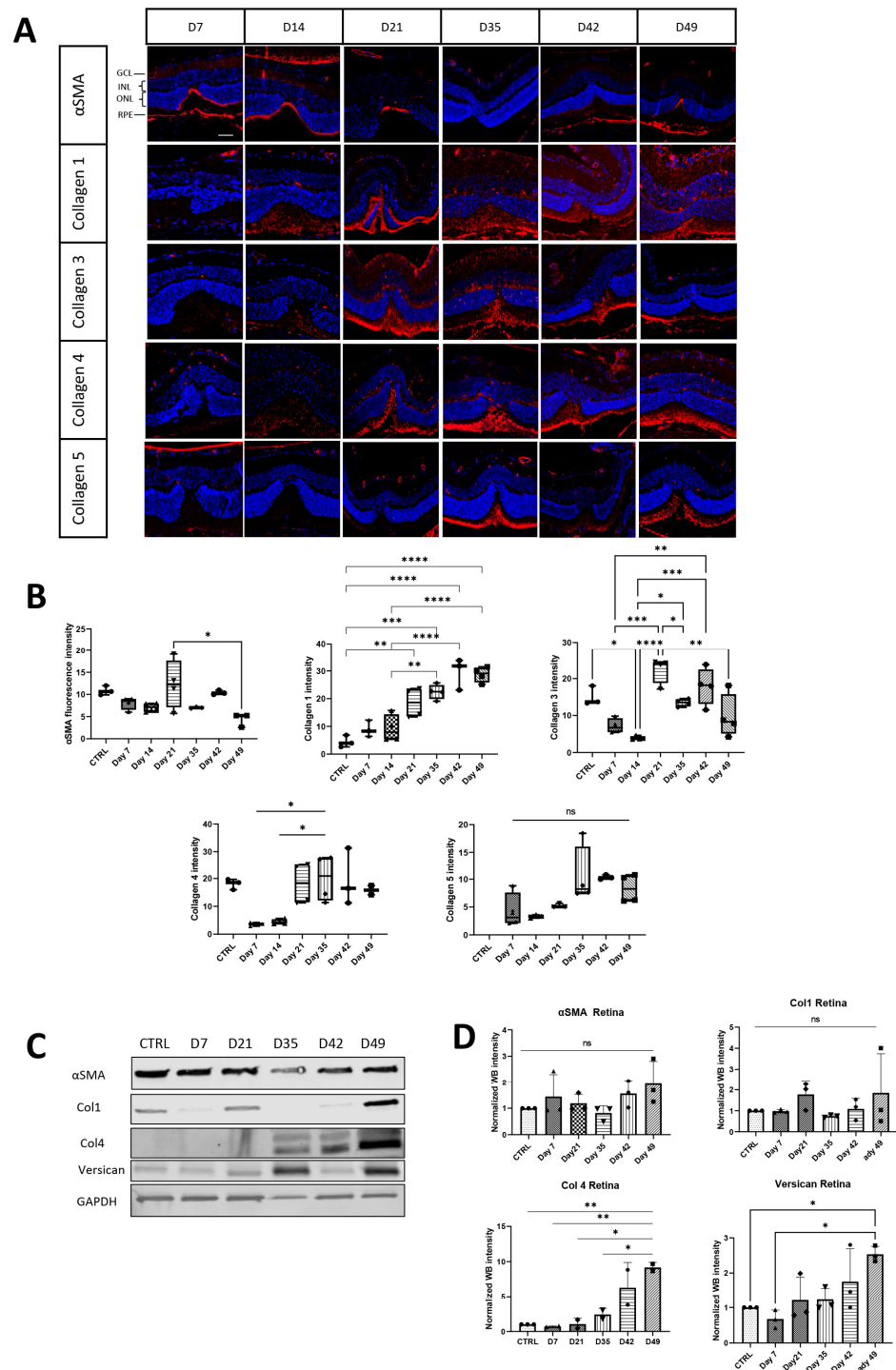


Figure 3. Time-dependent expression of α SMA and major component of ECM proteins in the retinas of control and laser-treated mice. **(A)** Retinal sections were stained with specific antibodies against α SMA and collagen 1, 3, 4, and 5 (red) and DAPI staining of the nuclei (blue), and fluorescence intensity was measured for each antibody in **(B)**. Scale bar is 50 μ m. **(C)** Western blot analysis was performed to quantify fibronectin, α SMA, collagen 1, collagen 4 and versican. **(D)** Statistical analysis was performed using one-way ANOVA with the Bonferroni multiple comparison test, and values are expressed as mean \pm SD. The study involved three mice per group, and significance levels were set at $p < 0.05$ *, $p < 0.01$ **, $p < 0.001$ ***, and $p < 0.0001$ ****, ns = not significant.

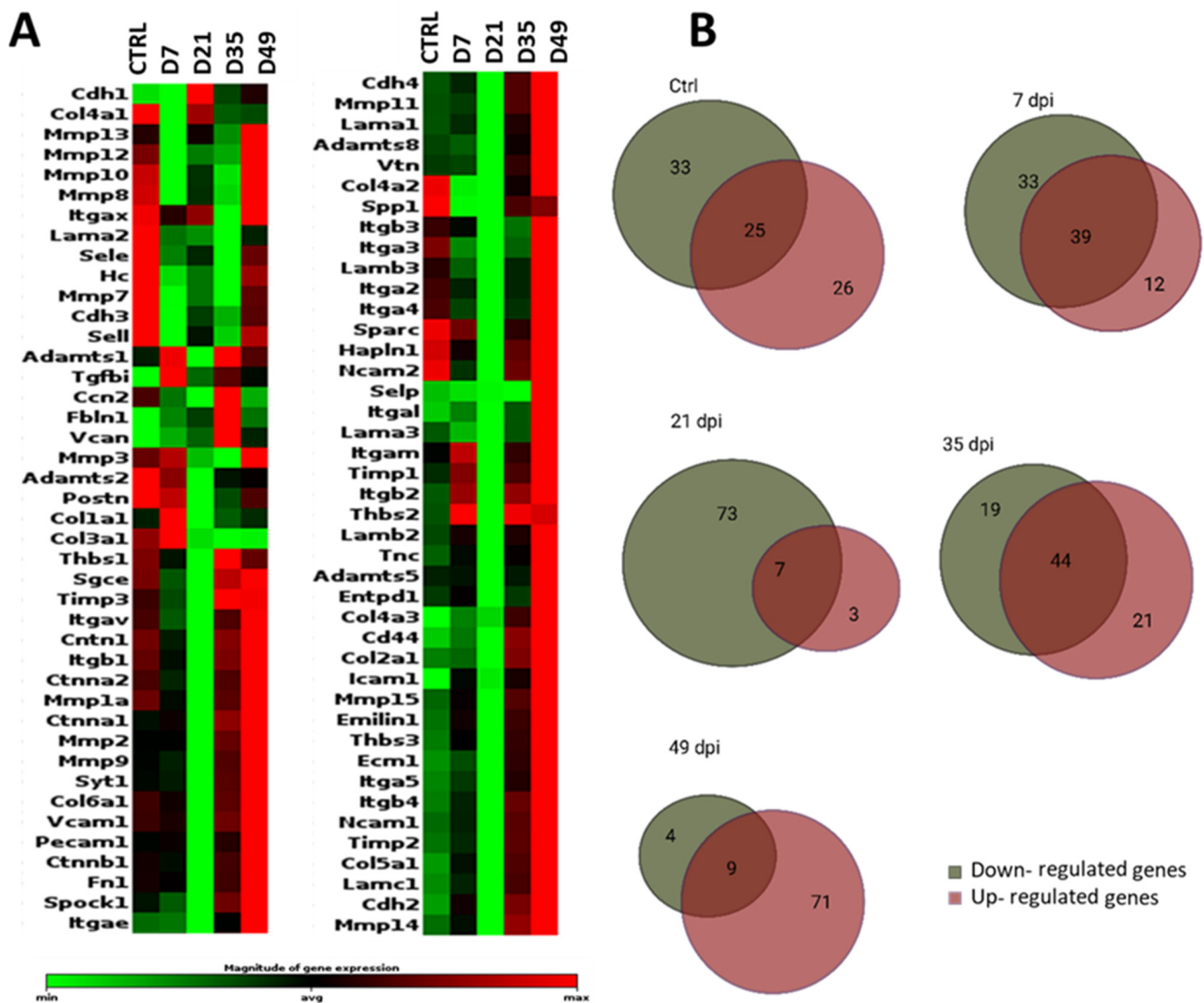


Figure 4. (A) Heatmap of ECM and adhesion molecule genes in murine retinas after laser injury at selected data collection points (CTRL, 7 dpi, 21 dpi, 35 dpi, 49 dpi). Differential gene expression in uninjured (CTRL) and injured retinas over time is shown. The RNA expression profile of grouped data from three mice (2 retinas pooled) per time point is shown as a heatmap graph. The data are displayed using a standard red–green map, with red indicating values above the mean, black indicating the mean, and green indicating values below the mean of a row (gene) across all columns (samples). The entire dataset is hierarchically clustered in a non-supervised manner in this clustergram, which displays a heatmap with dendrograms that show co-regulated genes. The marked area on the magnitude expression bar shows the defined average area for categorizing gene expression as upregulated, downregulated, or neutral. (B) Venn diagrams summarize gene expression per time point grouped in upregulated, downregulated, or neutral genes.

3.2.3. Transmembrane Molecules and Adhesion Molecules

Another separate group of transmembrane and adhesion molecule proteins contained 35 genes. On day 7, 18 of these genes were upregulated compared to the CTRL. However, only *Icam1* was substantially upregulated ($n = 3$, $p = 0.05$; Figure 5D,E; Supplementary Table S2). The only upregulation at day 21 was found with *Cdh1* ($n = 3$, $p > 0.05$). *Cdh2*, *Icam1*, *Itga5*, *Itgb4*, *Mmp14*, and *Mmp15* were upregulated on day 35 ($n = 3$, $p > 0.05$), while *Cdh3*, *Sele*, and *Sell* were significantly downregulated ($n = 3$, $p > 0.05$). The highest upregulation was shown on day 49 post-laser; 23 of 29 genes in this subgroup were higher compared to CTRL (*Selp* and *Itgal* significantly $n = 3$, $p = 0.03$).

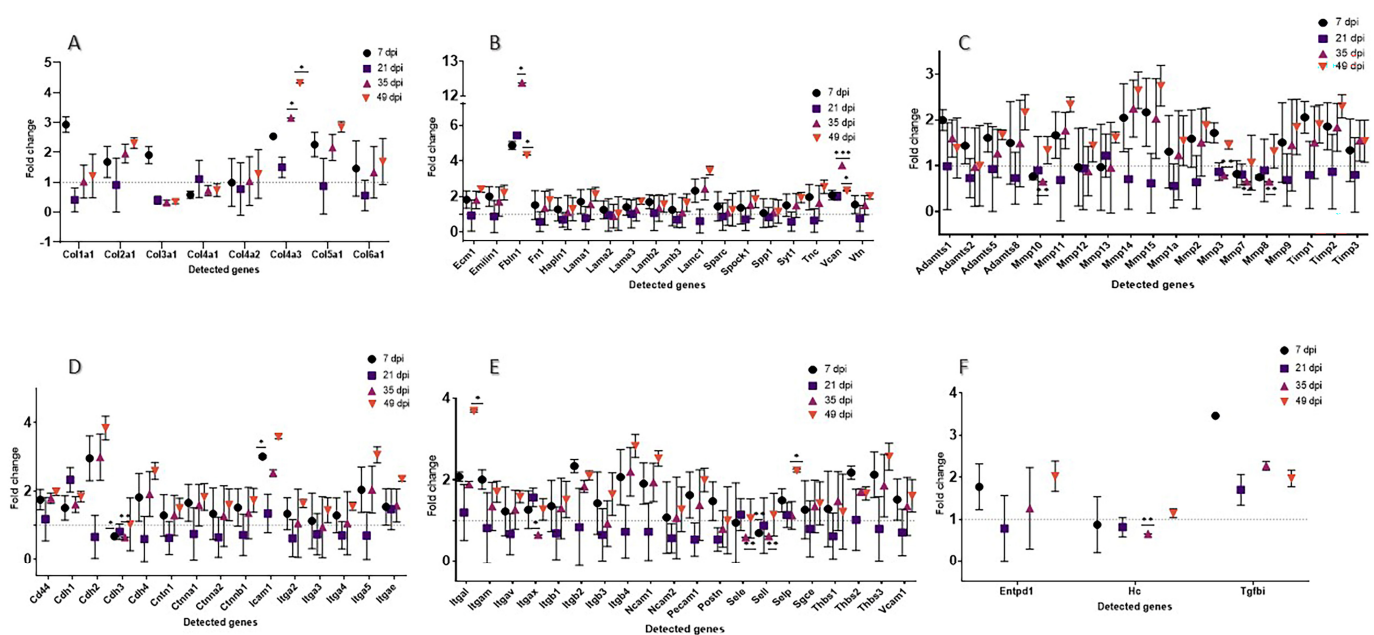


Figure 5. Fold change of RT2 mouse assay lasered mouse retinas. (A,B): ECM components, (C) ECM protease and inhibitors, (D,E) transmembrane and adhesion molecules, (F) other ECM proteins. For statistical analysis, the p -value was computed using Student's t -test, which employs a parametric, unpaired, two-sample equal variance. * $p > 0.05$, ** $p > 0.01$, *** $p > 0.001$.

3.2.4. Proteases and Inhibitors

Of the 19 protease and inhibitor genes investigated, only three showed significant differences compared to CTRL at any time point. However, *Timps1*, *Timps2*, and *Mmp11* were upregulated on day 7 ($n = 3$, $p \leq 0.05$). Furthermore, *Mmp10*, *Mmp3*, *Mmp7*, and *Mmp8* showed a downregulation at day 35 post-laser ($n = 3$, $p \leq 0.05$), while *Adamts8* and *Mmp11* were upregulated but without significance on day 49 post-laser. *Mmp15* and *Mmp14* showed a trend of upregulation at all selected time points, except on day 21 post-laser (Figure 5C; Supplementary Table S3).

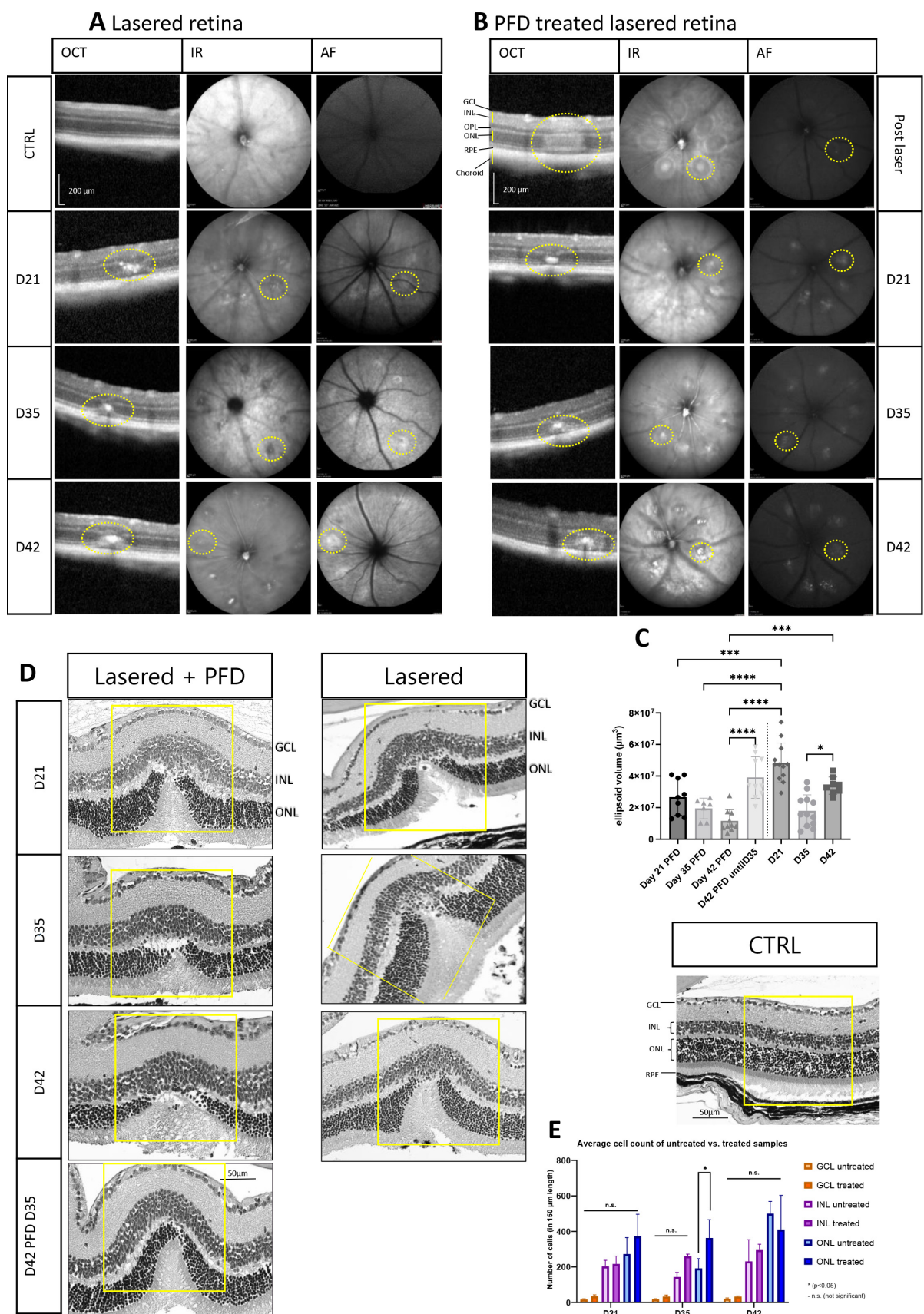
3.2.5. Other ECM Proteins

Three genes included in the array (*Entpd1*, *Hc*, *Tgfb1*) did not fit in any of the previously mentioned groups and were gathered separately. None showed significant differences compared to CTRL at any time point. *Tgfb1* shows a trend for upregulation at day 7 ($n = 3$, $p = 0.06$) and also on the other measured time points (Figure 5F; Supplementary Table S4). Also, *Entpd1* showed post-laser upregulation on day 7 and on day 49 ($n = 3$, $p \leq 0.05$).

3.3. Extracellular Matrix and Fibrosis Development after Treatment with Pirfenidone

3.3.1. Treatment with Pirfenidone Alters the Cell Count in the Outer Nuclear Layer and Results in Reduced Scar Formation

To determine whether PFD changed the lesion size, we quantified the volume of the laser spot with OCT measurements (b-scan, IR or AF). Comparing all collected data points of PFD-treated samples with lasered-only animals (CTRL and days 21, 35, and 42), we observed reduction in lesion size (Figure 6A,B). Thus, a significant reduction among all PFD samples was observed on day 21 as well as on day 42 when comparing treated versus untreated samples. Interestingly, when PFD treatment ended on day 35 post-laser, the lesion size increased again until day 42 to a size comparable to the untreated sample (Figure 6C). Additional H&E was performed at the selected time points to analyze cell numbers in the GCL, INL, and ONL over time (Figure 6D,E). By treating animals with PFD, a significant increase of nuclei could be only detected in the ONL at day 35.



as hyper-reflective spot (yellow outlined). (C) The ellipsoid volume was analyzed with one-way ANOVA with the Bonferroni multiple comparisons test for $p = 0.05$ *, $p = 0.0001$ ***, $p < 0.0001$ ****. (D) Hematoxylin and eosin staining showed thinning of the retina. (E) Quantification of cell nuclei in ONL, INL, and GCL in lasered and additional PFD treated samples was determined using one-way ANOVA with the Bonferroni multiple comparisons test for $p = 0.05$ * and n.s. (not significant). Scale bar is 50 μm .

3.3.2. Pirfenidone Prevents Changes in Collagen Expression during Fibrotic Development

To characterize the changes in fibrotic response after PFD treatment, we harvested retinas at days 21, 35, and 42 post-laser to perform WB, rtPCR, and IHC. After drug treatment, we found a reduction in collagen expression as shown in Figure 7. Levels of collagen types 1, 3, and 4 were unchanged compared to non-lasered controls (Figure 7A,B) and showed no increase in collagen expression as found without PFD treatment as previously depicted (Figure 3). In line with these findings, quantitative Western blot analysis confirmed no significantly changed collagen protein levels in the PFD-treated samples over time. Furthermore, Western blot data showed comparatively low collagen levels, as seen in IHC (Figure 7C,D). Similar protein levels were observed for fibronectin with both Western blot and IHC at all measured time points compared to intact retina control samples. The inhibitory effect of PFD on the immune response yielded no significant changes in IL-1 β expression, either on the protein or the gene level compared to CTRL samples (Figure 7A,E). This is in contrast to previously detected changes after laser treatment (Figure 2). However, the activated myofibroblast marker αSMA was increased and localized in the damaged area at all measured time points until day 42 post-laser. Nevertheless, neither Western blot analysis nor IHC showed significantly higher protein levels and fluorescence intensity compared to the CTRL.

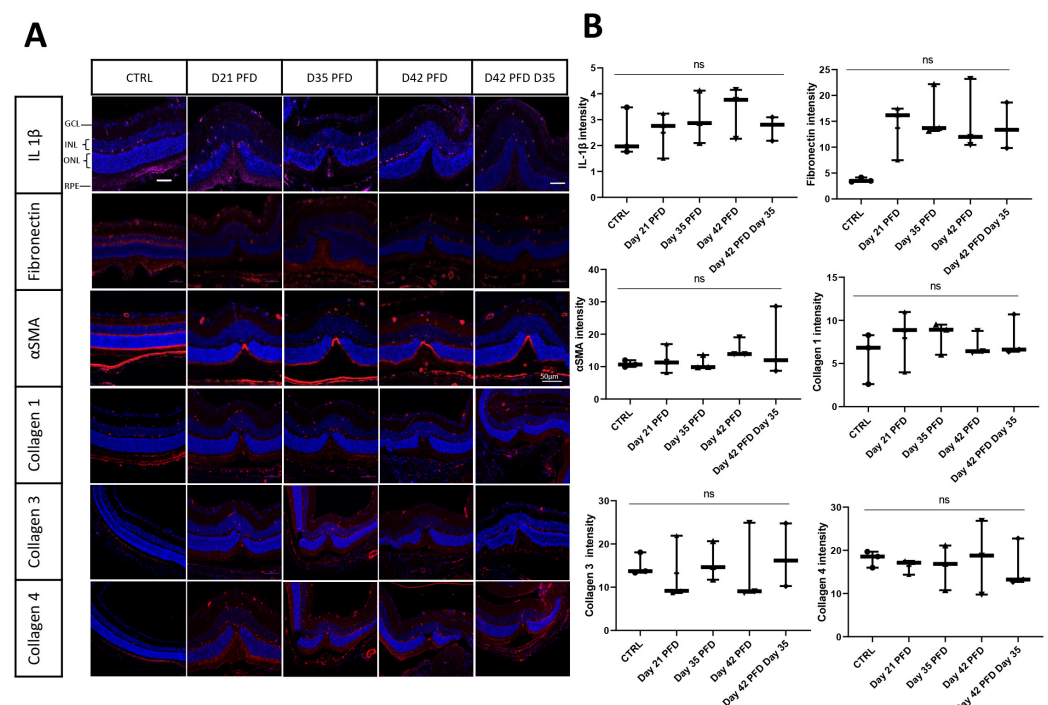


Figure 7. Cont.

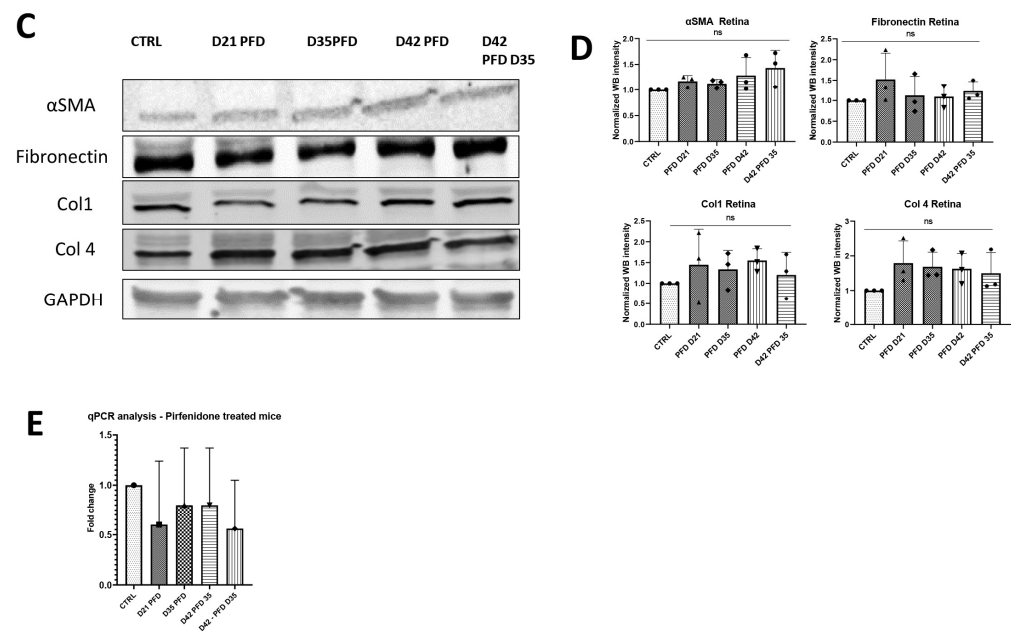


Figure 7. Time-dependent retinal expression of ECM markers. (A) Representative retinal section of control (CTRL) and lasered retina on selected time points stained with specific antibodies against IL-1 β , fibronectin, α SMA, and collagens 1, 3, 4, and 5 (red) shown as merged images with DAPI staining (blue). Scale bar is 50 μ m. (B) Fluorescence intensity is shown in addition to staining for each antibody. (C) Western blot analysis of fibronectin, α SMA, collagen 1, and collagen 4 was performed. Relative protein quantification did not show significant changes of the investigated markers (D). (E) mRNA expression of IL-1 β showed no significant changes compared to control (CTRL). ns = not significant.

3.3.3. Screening of ECM and Adhesion Molecules Involved in the ECM Formation during Damage Response after PFD Treatment

Herein, we analyzed gain the 84 genes related to fibrotic response and extracellular matrix performance (see Table 1) to show the influence of PFD on ECM formation at the selected data points (CTRL, day 21 PFD, day 35 PFD, day 42 PFD, and D42 PFD D35).

3.3.4. General Comparisons

Among the 84 genes studied after PFD treatment, we found a balanced expression of proteins with similar numbers of up- and downregulated genes. At day 21, 27 genes were downregulated and 26 genes were upregulated, whereas 28 genes were downregulated and 27 genes were upregulated at day 42 (Figure 8). Of these time-listed genes, 15 showed statistically significant differences compared to CTRL at the selected time points ($n = 3$, $p > 0.05$). Two genes (*Col3a1* and *Col4a1*) showed a significant downregulation and three genes (*Mmp8*, *Selp*, and *Tgfbi*) showed a significant upregulation ($n = 3$, $p > 0.05$) at all time points (Figure 9).

3.3.5. Extracellular Matrix Components

Col3a1 and *Col4a1* were significantly downregulated compared to the CTRL ($n = 3$, $p > 0.05$), as was *Lama2*, but without significance ($n = 3$, $p > 0.05$), at all time points (Figure 9A,B; Supplementary Table S1). The analysis showed significant upregulation of *Col4a2* and *Lama2* on day 21. Moreover, *Col1a1*, *Lamb3*, and *Col4a3* showed an upregulation at all selected time points ($p \leq 0.05$). Both PFD treated animal groups until day 42 were analyzed and depicted an upregulation for *Col1a1* without significance. *Emilin1* showed a trend and was slightly increased at all observed time points ($p = 0.8$).

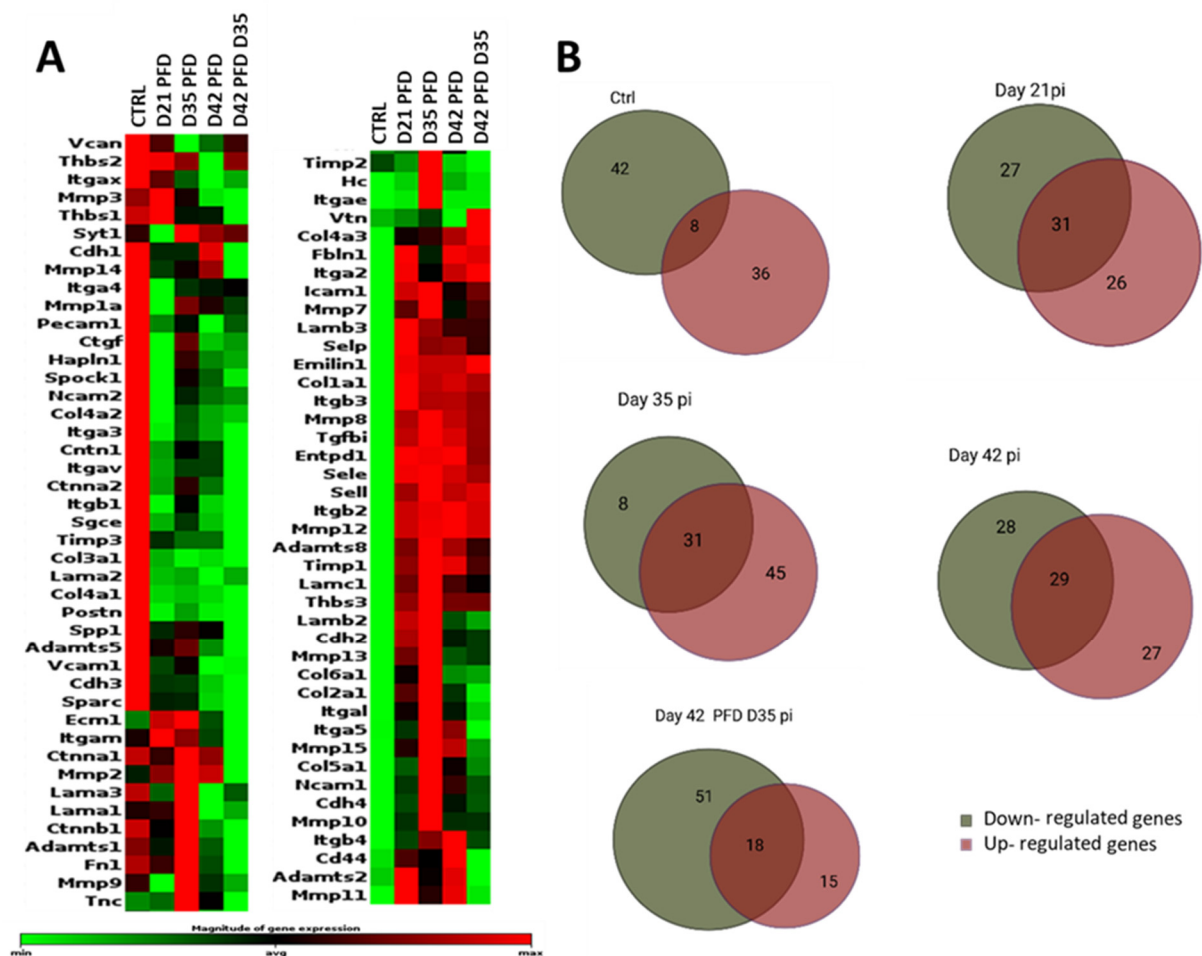


Figure 8. (A) Heatmap for ECM components and adhesion molecules in murine retinas after laser injury at selected time points (day 21 PFD, Day 35 PFD, Day 42 PFD, and Day 42 PFD D 35 post injury). Differential gene expression in normal (CTRL) and injured retinas over time is shown. Grouped data from three mice (2 retinas pooled) per time point are shown. The data are displayed using a standard red-green-map, with red indicating values above the mean, black indicating the mean, and green indicating values below the mean of a row (gene) across all columns (samples). Marked area on the magnitude expression bar shows defined average area for grouping gene expression into upregulated, downregulated, or neutral. (B) Venn diagrams summarize gene expression per time point grouped by upregulated, downregulated, or neutral genes.

3.3.6. Transmembrane Molecules and Adhesion Molecules

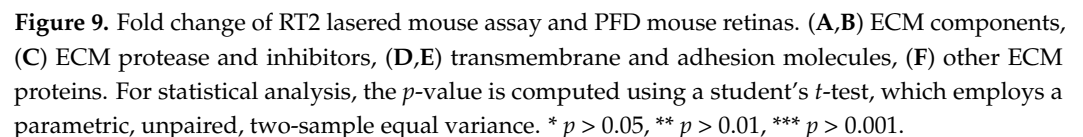
Of the 34 genes, *Itgb2*, *Itgb3*, *Sele*, *Sell*, and *Selp* were upregulated at all time points. *Sele*, *Itgb2*, and *Itgb3* showed a trend and were increased on day 21, day 42, and day 42 PFD day 35. *Sell* was increased for both samples of day 42 ($n = 3$, $p \leq 0.05$), while *Selp* showed significant upregulation at all time points ($p = 0.02$; Figure 9E,F; Supplementary Table S6).

3.3.7. Proteases and Inhibitors

Mmp8 was significantly upregulated at all time points, as was Mmp12, but only significantly at day 21 and D42 PFD D35 (Figure 9C; Supplementary Table S7). Furthermore, the *Timp* genes showed a non-significant upregulation at all measured time points ($n = 3$, $p > 0.05$).

3.3.8. Other ECM Proteins

Only *Tgfb1* was significantly upregulated at all measured time points compared to the CTRL ($n = 3$, $p > 0.05$; Figure 9F; Supplementary Table S8).



Retinal wound repair is a complex process which involves interconnected biological mechanisms, including inflammation, cell proliferation, and tissue remodeling. In general, four overlapping phases in the process of general wound healing have been defined. The first phase is characterized by hemostasis, during which the bleeding is stopped. The second phase is an immediate inflammatory response that involves the infiltration of leukocytes, which release cytokines with antimicrobial properties. These cytokines activate the third phase, the proliferative phase, in which, among other processes, new ECM is generated. Finally, in the fourth phase, the wound contracts over a period of weeks to months as the ECM is restructured [25]. These specific changes to the ECM during remodeling of the retina after the loss of photoreceptors are dependent on a complex of several cellular and molecular components, which are not fully understood. Thus, the function of the ECM is not only structural support, but also regulation of fluid and solute passage from the choroid to the retina. In this study, the expression of key ECM components after laser-induced damage in adult mouse retinas was investigated by inducing the photoreceptor degeneration and retinal thinning that occurs in many retinal diseases. This time-dependent model enabled spatial observation of internal processes during retinal scarring caused by photoreceptor loss. The laser model employed herein differs from a recently published CNV model, which leads to subretinal fibrosis [26]. In comparison, the subretinal fibrosis model published by Zandi et al., we showed absence of neovascularization at all time points post-laser by negative isolectin B4 staining. In contrast, therein an increase in CNV until day 14 and a regression of CNV with an increase of subretinal fibrosis after day 21 post injury by initially rupturing Bruch's membrane and inducing a characteristic bubble, was displayed.

Current research has shown that several types of retinal cells, including RPE cells, endothelial cells, epithelial cells, Müller cells, and macrophages, have the ability to transform into myofibroblasts. These myofibroblasts are the primary cell type responsible for

triggering fibrosis and producing ECM components [1,27,28]. They also express α -SMA, a filamentous contractile protein, during their activation state and their persistent stimulation is associated with excessive ECM deposition leading to organ dysfunction [29]. Our data show that α -SMA expression displays biphasic kinetics after laser-induced retinal damage. However, as shown in the unlasered control, α -SMA is also present in the choroidal space under normal physiological conditions, where it plays a pivotal role in regulating vascular diameter, vascular tone, and retinal blood flow [30].

One primary response of wound healing is acute inflammation through recruitment of immune cells and fibroblasts to the site of tissue damage. However, effective wound repair necessitates the resolution of inflammation, while an excessive inflammatory response can lead to the formation of retinal scars [31]. In our model, we showed the development of three stages of cytokine secretion indicating several waves of inflammation. Firstly, an initial IL-1 β production within 24 h post injury. Second, an intermediate phase with no difference compared to baseline amounts. Finally, a repeated biphasic increase was noted on days 21 and 42. Tissue with regenerative potential resolves the inflammatory response within a few days with the removal of myofibroblasts and inflammatory macrophages, so that the scar gradually breaks down within several weeks [27]. In wet AMD, the connection between inflammation and abnormal blood vessel growth is well known [1]. In dry AMD, the role of inflammation caused by drusen formation due to accumulation of toxic debris, such as lipofuscin, has been found to form a chronic and toxic milieu for RPE cells, thus creating a pro-inflammatory microenvironment [32]. As we did not induce CNV lesions that actively destabilize the Bruch's membrane and had no drusen formation as inflammatory mediators in our mouse model, our data indicate repeated release of IL-1 β in the damaged area. This might lead to the destabilizing of the BRB and leukocyte infiltration. It is also known that macroglia cells show upregulation of the pro-inflammatory cytokine S100 β under stress conditions and microglia are initiators of chronic scarring [33]. However, the observed three-phasic inflammation signal influences the fibrotic response towards chronic scar formation and hindering therewith any repair process. As one of the earliest ECM matrix proteins, fibronectin appears 10 min post injury and was recently described as an inflammatory mediator [25,34]. Fibronectin expression in the RPE layer peaks at early and late stages of wound repair in the injured area. We therefore hypothesize that inflammatory mediators are active in the RPE layer as well as in retinal cells so that the complex architecture of the ECM is continuously synthesized.

Since collagens are the key components of a healing wound and are the most prominent proteins of the ECM scaffold, we investigated the appearance of collagen types 1, 3, 4, and 5 via immunochemistry. While collagen types 1, 3, and 5 belong to the group responsible for fiber formation with long ropelike structures and assemble into polymers; collagen type 4 stands out as the primary constituent of the basement membrane, possesses the ability to organize into sheet-like networks within this structure [35]. Increased expression was detectable for collagen 1 from day 14, for collagen 3 from day 21, and for collagens 4 and 5 from day 35 on. The expression of all analyzed collages was found until day 49 post-laser.

Similar to the observed inflammation marker IL1 β , collagens showed a wavelike expression. Compared to findings in other tissues, including the skin, heart and liver, our results diverge from reported observations regarding a shift in the collagen 1 to collagen 3 ratio. These changes typically manifest as an increased concentration of collagen 3 during the healing phase, followed by a subsequent rise in collagen 1 content in the healed tissue [36]. On the other hand, our data indicate a substantial presence of collagen types 1 and 3 persisting until the last recorded time point on day 49. This suggests a notable constraint on wound healing, with no discernible indications of regenerative processes. The gene expression levels showed significant increase only for Col4a3, even with the majority of collagens upregulated at day 7 and day 35 post-laser. This result fits the characteristics of the retina as a collagen 4-rich tissue which is mainly found in the Bruch's membrane and the inner limiting membrane and is critical for neuronal survival and angiogenesis [37].

On the other hand, its abnormal deposition is seen in fibrotic lesions of certain organs, including the kidneys and lungs [38,39].

Herein, we provide an overview of the complex ECM formation in our injury model and show that the most robust alterations in gene expression were detected for Col4 α 3, fibulin1 (Fbln1), cadherin 3 (Cdh3), intracellular adhesion molecule-1 (Icam1), integrin alpha L (Itgal), selectin E (Sele), transforming growth factor beta-induced (Tgfb1), and versican (Vcan). Except Cdh3 and Sele, all genes were significantly upregulated, mainly at day 35 and day 49 post-laser in the late stage of retinal fibrosis. Most of these genes indicate a causal role for leucocyte infiltration during the regenerative phase, which might inhibit remodeling. The observed upregulation of Fibulin 1 in our wound healing model corresponds to a study on patients with pulmonary fibrosis. This study identified the bioactive region/s of fibulin-1C responsible for promoting fibrosis, indicating potential shared mechanisms in fibrotic processes [40]. A binding partner of fibulin 1 is versican, a member of the hyalactin family of ECM components. In the retina, similar to the brain, ECM is formed from proteoglycan proteins, such as versican (Vcan), to implement the three-dimensional network of extracellular macromolecules. In most diseases, including lung disease and several different cancers, these proteoglycans increase dramatically during inflammation [41]. Our data concurred, as we observed Vcan upregulation in the late stage of tissue response. The literature indicates that neurons and glial cells might synthesize proteoglycans and glycoproteins together with fibrous proteins, such as collagens and fibronectin [42]. Thus, proteoglycan as well as P- and L-selectins increase dramatically during inflammation and interacts with receptors that are found on the surface of immune cells [43–45]. According to existing literature, the ECM exhibits an organization into cable-like structures involving versican and other proteins, including hyaluronan, which bind to leukocytes. Further investigations are warranted to elucidate the specific contributions of these complex components to the phenotype of leukocytes.

Furthermore, the upregulation of the protein Icam 1 is particularly essential for the migration of leukocytes and has been described in several ocular diseases, such as diabetic retinopathy and CNV [46]. In other organs, such as the liver, Icam 1 has been described as an inflammatory and fibrotic marker [47]. We could detect two peaks for Icam 1 expression at the gene level, namely on day 7 and day 49 post-laser. These findings could imply not only leukocytes entering the retina but also their role in fibrosis. Another marker, Itgal, was significantly upregulated on day 49 post-laser. This gene encodes integrin components, including lymphocyte function-associated antigen 1 (LFA-1), which are expressed on lymphocytes to participate in immune and inflammatory responses [27]. In contrast, Cdh3 (also known as P-cadherin) was significantly downregulated on day 7 and day 35 post-laser. Previous publications have shown that Cdh3 is the dominant cadherin in mature RPE cells [48]. It plays a critical role in maintaining the structural integrity of epithelial tissues, regulating processes involved in embryonic development, and maintaining adult tissue architecture and cell differentiation. The downregulation of Cdh3 suggests a decreased density of RPE after laser damage. Thus, the two-wave dynamic of Cdh3 downregulation might indicate a destabilized RPE layers, leading to higher permeability with migration of peripheral immune cells. Cdh3 might also influence stem cell activity. Earlier studies have reported a significant loss of epithelial progenitor cells and downregulation of putative stem cell markers in organ-cultured limbal tissue [49].

To modulate the laser-induced damage including fibrosis and ensuing immune response, we used PFD, which is not only anti-inflammatory but has anti-fibrotic properties also. PFD inhibits fibroblast proliferation and the production of fibrosis-associated proteins and cytokines that increase the biosynthesis of ECM proteins, such as collagen and fibronectin. Such cytokine secretion is mediated by TGF- β or PDGF pathways [50]. Despite demonstrating a reduced expression of collagen 1, 3, 4 and 5 and IL-1 β after PFD treatment, we were not able to detect long-term effects on the scar tissue. This finding suggests a yet-undefined time window in which inflammation must be prevented or halted. Otherwise, even after the inhibition of inflammation and reduction of fibrotic signals, fibrosis inevitably

occurs [51]. Day 14 post-laser is likely already too late as the starting point for inhibition of fibrosis development and modulation. Alternatively, additional pro-inflammatory cytokines are produced, or inflammation is not downregulated in general. Tissue with limited regenerative capacity, such as the retina, has a high risk for repetitive fibrotic responses or chronic developments with aggregation of ECM, myofibroblasts, and macrophages [52]. Examining the expression of involved genes, we found a shifting of gene expression toward 12 pro-fibrotic genes after PFD treatment compared to non-treated samples. Thus, *Col3α1* and *Col4α1* were downregulated, whereas *Itgb2* and *Itgb3* were upregulated.

The selectin family, composed of L-selectin (SELL), E-selectin (SELE), and P-selectin (SELP), plays a significant role in mediating cell adhesion. Most leukocytes express L-selectin, while activated endothelial cells express E-selectin and P-selectin [53,54]. All three family members were significantly upregulated after PFD treatment. Based on our hypothesis, the drug treatment might have activated endothelial cells in the surrounding blood vessels which facilitate leukocyte infiltration by assisting in their adhesion and subsequent transportation into the retinal layers, thereby influencing remodeling processes.

The expression of transforming growth factor beta induced (*Tgfb1*), which is regulated by TGF-β signaling, was significantly upregulated at all detected time points. The ability of *Tgfb1* to bind to ECM proteins, such as fibronectin, laminin, vitronectin, and collagens, is likely due to fasciclin 1 (*FAS1*) [55].

Matrix metalloproteinases (MMPs) are a class of enzymes responsible for breaking down ECM and regulating ECM turnover and homeostasis. Tissue inhibitors of metalloproteinases (TIMPs) are specific inhibitors of MMPs that bind to active MMPs and inhibit the process of ECM degradation. Previous research has shown that excessive expression of TIMP-1 may hinder wound healing by impeding epithelial cell migration, a critical aspect of re-epithelialization [56]. Although we observed an upregulation of *Timp1* levels at all selected time points after PDF treatment, this upregulation was not significant.

We showed that, inflammation peaks on day 1, day 21 and day 49 in the used laser-based retina degeneration model. This inflammation hindered remodeling as fibrosis continued over 49 days post-laser treatment. Our findings suggested that *Cdh3* downregulation in the late stage might explain the absence of stem cell activation or proliferative capacity in the mouse retina.

5. Conclusions

In conclusion, our data identify a three-phasic inflammation during retinal degeneration and scar formation, detect significant changes in gene expression of ECM-related genes during retinal wound healing with *Col4α3*, *ICAM1*, *fibulin1*, *itgal* and *selp* as involved key genes, and shows that pirfenidone reduces the expression of ECM proteins and inflammatory markers but may not prevent long-term fibrotic responses. The study had some limitations, as the focus lay mainly on the mRNA expression in lasered retina samples. The samples showed a limited amount of laser damage that might explain the low significance for most of the detected genes. Additionally, we did not focus on changes in the surrounding tissues (e.g., choroid) during scarring, which may also be part of the interaction between ECM/adhesion molecules and, especially, the involved cells. However, the employed laser model of retinal degeneration mimics disease phenotypes in humans histologically as well as regarding its gliotic/fibrotic changes [57]. Still, further studies are needed to validate our findings and conjectures in vivo.

Supplementary Materials: The following supporting information can be downloaded at: <https://www.mdpi.com/article/10.3390/cells13020164/s1>, Figure S1: Isolectin GS-B4 staining for CNV detection without Bruch's membrane rupture after modification of the laser setting; Table S1: Fold change of ECM component proteins post-lasered samples; Table S2: Transmembrane and adhesion molecules fold change laser treated samples; Table S3: Fold change data of ECM protease and inhibitors post-laser; Table S4: Fold change of other ECM proteins post-laser; Table S5: Fold change of ECM components PFD samples; Table S6: Fold change of Transmembrane and adhesion molecules PFD

samples; Table S7: Fold change of ECM protease and inhibitors PFD samples; Table S8: Fold change of other ECM proteins PFD samples.

Author Contributions: Conceptualization, L.J. and V.E.; formal analysis, L.J. and S.Z.; investigation, L.J., V.P., S.Z., Y.L. and V.E.; methodology, Y.L. and F.M.C.; resources, V.E.; writing—original draft preparation, L.J.; writing—review and editing, S.Z., F.M.C. and V.E.; visualization, L.J. and S.Z.; supervision, V.E.; project administration, V.E.; funding acquisition, V.E. All authors have read and agreed to the published version of the manuscript.

Funding: This research was partially funded by the Hanel-Stiftung, Aarau, Switzerland.

Institutional Review Board Statement: The animal study protocol was approved by the governmental authorities of the Canton of Bern (BE 146/2020 from 15 March 2021).

Informed Consent Statement: Not applicable.

Data Availability Statement: All the data have been included in Supplementary Materials.

Acknowledgments: The authors thanks Anelia Schweri-Olac for outstanding technical assistance. This work was kindly supported by the MIC imaging facility of the Dept. of BioMedical Research, University of Bern, especially by Selina Steiner and Carlos Wotzkow.

Conflicts of Interest: The authors declare no conflict of interest.

References

- Ishikawa, K.; Kannan, R.; Hinton, D.R. Molecular mechanisms of subretinal fibrosis in age-related macular degeneration. *Exp. Eye Res.* **2016**, *142*, 19–25. [\[CrossRef\]](#) [\[PubMed\]](#)
- Gabbiani, G. The myofibroblast in wound healing and fibrocontractive diseases. *J. Pathol.* **2003**, *200*, 500–503. [\[CrossRef\]](#)
- Van Leeuwen, E.M.; Emri, E.; Merle, B.M.J.; Colijn, J.M.; Kersten, E.; Cougnard-Gregoire, A.; Dammeier, S.; Meester-Smoor, M.; Pool, F.M.; de Jong, E.K.; et al. A new perspective on lipid research in age-related macular degeneration. *Prog. Retin Eye Res.* **2018**, *67*, 56–86. [\[CrossRef\]](#) [\[PubMed\]](#)
- Litwińska, Z.; Sobuś, A.; Łuczkowska, K.; Grabowicz, A.; Mozolewska-Piotrowska, K.; Safranow, K.; Kawa, M.P.; Machaliński, B.; Machalińska, A. The Interplay Between Systemic Inflammatory Factors and MicroRNAs in Age-Related Macular Degeneration. *Front. Aging Neurosci.* **2019**, *11*, 286. [\[CrossRef\]](#) [\[PubMed\]](#)
- Wooff, Y.; Man, S.M.; Aggio-Bruce, R.; Natoli, R.; Fernando, N. IL-1 Family Members Mediate Cell Death, Inflammation and Angiogenesis in Retinal Degenerative Diseases. *Front. Immunol.* **2019**, *10*, 1618. [\[CrossRef\]](#) [\[PubMed\]](#)
- Natoli, R.; Fernando, N.; Madigan, M.; Chu-Tan, J.A.; Valter, K.; Provis, J.; Rutar, M. Microglia-derived IL-1 β promotes chemokine expression by Müller cells and RPE in focal retinal degeneration. *Mol. Neurodegener.* **2017**, *12*, 31. [\[CrossRef\]](#) [\[PubMed\]](#)
- Spindler, J.; Zandi, S.; Pfister, I.B.; Gerhardt, C.; Garweg, J.G. Cytokine profiles in the aqueous humor and serum of patients with dry and treated wet age-related macular degeneration. *PLoS ONE* **2018**, *13*, e0203337. [\[CrossRef\]](#)
- Miller, J.W. Beyond VEGF-The Weisenfeld Lecture. *Investig. Ophthalmol. Vis. Sci.* **2016**, *57*, 6911–6918. [\[CrossRef\]](#)
- Viviani, B.; Corsini, E.; Binaglia, M.; Galli, C.L.; Marinovich, M. Reactive oxygen species generated by glia are responsible for neuron death induced by human immunodeficiency virus-glycoprotein 120 in vitro. *Neuroscience* **2001**, *107*, 51–58. [\[CrossRef\]](#)
- Viviani, B.; Bartesaghi, S.; Gardoni, F.; Vezzani, A.; Behrens, M.M.; Bartfai, T.; Binaglia, M.; Corsini, E.; Di Luca, M.; Galli, C.L.; et al. Interleukin-1 β Enhances NMDA Receptor-Mediated Intracellular Calcium Increase through Activation of the Src Family of Kinases. *J. Neurosci.* **2003**, *23*, 8692–8700. [\[CrossRef\]](#)
- Wang, H.; Han, X.; Wittchen, E.S.; Hartnett, M.E. TNF- α mediates choroidal neovascularization by upregulating VEGF expression in RPE through ROS-dependent β -catenin activation. *Mol. Vis.* **2016**, *22*, 116–128.
- Alshoubaki, Y.K.; Nayer, B.; Das, S.; Martino, M.M. Modulation of the Activity of Stem and Progenitor Cells by Immune Cells. *Stem Cells Transl. Med.* **2022**, *11*, 248–258. [\[CrossRef\]](#) [\[PubMed\]](#)
- Olivares-González, L.; Velasco, S.; Campillo, I.; Rodrigo, R. Retinal Inflammation, Cell Death and Inherited Retinal Dystrophies. *Int. J. Mol. Sci.* **2021**, *22*, 2096. [\[CrossRef\]](#)
- Gao, C.; Cao, X.; Huang, L.; Bao, Y.; Li, T.; Di, Y.; Wu, L.; Song, Y. Pirfenidone Alleviates Choroidal Neovascular Fibrosis through TGF- β /Smad Signaling Pathway. *J. Ophthalmol.* **2021**, *2021*, 8846708. [\[CrossRef\]](#) [\[PubMed\]](#)
- Ma, W.; Silverman, S.M.; Zhao, L.; Villasmil, R.; Campos, M.M.; Amaral, J.; Wong, W.T. Absence of TGF β signaling in retinal microglia induces retinal degeneration and exacerbates choroidal neovascularization. *eLife* **2019**, *8*, e42049. [\[CrossRef\]](#) [\[PubMed\]](#)
- Hewitson, T.D.; Kelynack, K.J.; Tait, M.G.; Martic, M.; Jones, C.L.; Margolin, S.B.; Becker, G.J. Pirfenidone reduces in vitro rat renal fibroblast activation and mitogenesis. *J. Nephrol.* **2001**, *14*, 453–460.
- Ruwanpura, S.M.; Thomas, B.J.; Bardin, P.G. Pirfenidone: Molecular Mechanisms and Potential Clinical Applications in Lung Disease. *Am. J. Respir. Cell Mol. Biol.* **2020**, *62*, 413–422. [\[CrossRef\]](#)
- Lopez-de la Mora, D.A.; Sanchez-Roque, C.; Montoya-Buelna, M.; Sanchez-Enriquez, S.; Lucano-Landeros, S.; Macias-Barragan, J.; Armendariz-Borunda, J. Role and New Insights of Pirfenidone in Fibrotic Diseases. *Int. J. Med. Sci.* **2015**, *12*, 840–847. [\[CrossRef\]](#)

19. Meng, X.-M.; Nikolic-Paterson, D.J.; Lan, H.Y. TGF- β : The master regulator of fibrosis. *Nat. Rev. Nephrol.* **2016**, *12*, 325–338. [[CrossRef](#)]
20. Diaz-Palamera, C.D.; Vidal-Paredes, I.A.; Navarro-Partida, J.; Cid-Hernandez, M.; Rosales-Rivera, L.C.; De la Rosa-Bibiano, R.; Monroy-Ramirez, H.C.; Santos, A.; Armendariz-Borunda, J. Topical Pirfenidone-Loaded Liposomes Ophthalmic Formulation Reduces Haze Development after Corneal Alkali Burn in Mice. *Pharmaceutics* **2022**, *14*, 316. [[CrossRef](#)]
21. Khanum, B.N.M.K.; Guha, R.; Sur, V.P.; Nandi, S.; Basak, S.K.; Konar, A.; Hazra, S. Pirfenidone inhibits post-traumatic proliferative vitreoretinopathy. *Eye* **2017**, *31*, 1317–1328. [[CrossRef](#)] [[PubMed](#)]
22. Talpan, D.; Salla, S.; Seidelmann, N.; Walter, P.; Fuest, M. Antifibrotic Effects of Caffeine, Curcumin and Pirfenidone in Primary Human Keratocytes. *Int. J. Mol. Sci.* **2023**, *24*, 1461. [[CrossRef](#)]
23. Bao, Y.; Huang, L.; Huang, X.; Gao, C.; Chen, Y.; Wu, L.; Zhu, S.; Song, Y. Pirfenidone ameliorates the formation of choroidal neovascularization in mice. *Mol. Med. Rep.* **2020**, *21*, 2162–2170. [[CrossRef](#)] [[PubMed](#)]
24. Shah, P.V.; Balani, P.; Lopez, A.R.; Nobleza, C.M.N.; Siddiqui, M.; Khan, S. A Review of Pirfenidone as an Anti-Fibrotic in Idiopathic Pulmonary Fibrosis and Its Probable Role in Other Diseases. *Cureus* **2021**, *13*, e12482. [[CrossRef](#)] [[PubMed](#)]
25. Tracy, L.E.; Minasian, R.A.; Caterson, E.J. Extracellular Matrix and Dermal Fibroblast Function in the Healing Wound. *Adv. Wound Care* **2016**, *5*, 119–136. [[CrossRef](#)]
26. Zandi, S.; Li, Y.; Jahnke, I.; Schweri-Olac, A.; Ishikawa, K.; Wada, I.; Nakao, S.; Zinkernagel, M.S.; Enzmann, V. Animal model of subretinal fibrosis without active choroidal neovascularization. *Exp. Eye Res.* **2023**, *229*, 109428. [[CrossRef](#)]
27. Zhao, Z.; Zhang, Y.; Zhang, C.; Zhang, J.; Luo, X.; Qiu, Q.; Luo, D.; Zhang, J. TGF- β promotes pericyte-myofibroblast transition in subretinal fibrosis through the Smad2/3 and Akt/mTOR pathways. *Exp. Mol. Med.* **2022**, *54*, 673–684. [[CrossRef](#)]
28. Shu, D.Y.; Butcher, E.; Saint-Geniez, M. EMT and EndMT: Emerging Roles in Age-Related Macular Degeneration. *Int. J. Mol. Sci.* **2020**, *21*, 4271. [[CrossRef](#)]
29. Hinz, B. Myofibroblasts. *Exp. Eye Res.* **2016**, *142*, 56–70. [[CrossRef](#)]
30. An, D.; Chung-Wah-Cheong, J.; Yu, D.Y.; Balaratnasingam, C. Alpha-Smooth Muscle Actin Expression and Parafoveal Blood Flow Pathways Are Altered in Preclinical Diabetic Retinopathy. *Investig. Ophthalmol. Vis. Sci.* **2022**, *63*, 8. [[CrossRef](#)]
31. Eming, S.A.; Krieg, T.; Davidson, J.M. Inflammation in Wound Repair: Molecular and Cellular Mechanisms. *J. Investig. Dermatol.* **2007**, *127*, 514–525. [[CrossRef](#)] [[PubMed](#)]
32. Damico, F.M.; Gasparin, F.; Scolari, M.R.; Pedral, L.S.; Takahashi, B.S. New approaches and potential treatments for dry age-related macular degeneration. *Arq. Bras. Oftalmol.* **2012**, *75*, 71–76. [[CrossRef](#)]
33. Donato, R.; Sorci, G.; Riuzzi, F.; Arcuri, C.; Bianchi, R.; Brozzi, F.; Tubaro, C.; Giambanco, I. S100B's double life: Intracellular regulator and extracellular signal. *Biochim. Biophys. Acta Mol. Cell Res.* **2009**, *1793*, 1008–1022. [[CrossRef](#)] [[PubMed](#)]
34. Budatha, M.; Zhang, J.; Schwartz, M.A. Fibronectin-Mediated Inflammatory Signaling Through Integrin $\alpha 5$ in Vascular Remodeling. *J. Am. Heart Assoc.* **2021**, *10*, e021160. [[CrossRef](#)]
35. Van Der Rest, M.; Garrone, R. Collagen family of proteins. *FASEB J.* **1991**, *5*, 2814–2823. [[CrossRef](#)] [[PubMed](#)]
36. Singh, D.; Rai, V.; Agrawal, D.K. Regulation of Collagen I and Collagen III in Tissue Injury and Regeneration. *Cardiol. Cardiovasc. Med.* **2023**, *7*, 5–16. [[CrossRef](#)]
37. Halfter, W.; Willem, M.; Mayer, U. Basement membrane-dependent survival of retinal ganglion cells. *Investig. Ophthalmol. Vis. Sci.* **2005**, *46*, 1000–1009. [[CrossRef](#)]
38. Tomino, Y.; Suzuki, S.; Azushima, C.; Shou, I.; Iijima, T.; Yagame, M.; Wang, L.N.; Chen, H.C.; Lai, K.N.; Tan, S.Y.; et al. Asian multicenter trials on urinary type IV collagen in patients with diabetic nephropathy. *J. Clin. Lab. Anal.* **2001**, *15*, 188–192. [[CrossRef](#)]
39. Urushiyama, H.; Terasaki, Y.; Nagasaka, S.; Terasaki, M.; Kunugi, S.; Nagase, T.; Fukuda, Y.; Shimizu, A. Role of $\alpha 1$ and $\alpha 2$ chains of type IV collagen in early fibrotic lesions of idiopathic interstitial pneumonias and migration of lung fibroblasts. *Lab. Invest.* **2015**, *95*, 872–885. [[CrossRef](#)]
40. Ge, Q.; Chen, L.; Jaffar, J.; Argraves, W.S.; Twal, W.O.; Phil Hansbro, P.; Black, J.L.; Burgess, J.K.; Oliver, B. Fibulin1C peptide induces cell attachment and extracellular matrix deposition in lung fibroblasts. *Sci. Rep.* **2015**, *5*, 9496. [[CrossRef](#)]
41. Wight, T.N.; Kang, I.; Evanko, S.P.; Harten, I.A.; Chang, M.Y.; Pearce, O.M.T.; Allen, C.E.; Frevert, C.W. Versican-A Critical Extracellular Matrix Regulator of Immunity and Inflammation. *Front. Immunol.* **2020**, *11*, 512. [[CrossRef](#)]
42. Song, I.; Dityatev, A. Crosstalk between glia, extracellular matrix and neurons. *Brain Res. Bull.* **2018**, *136*, 101–108. [[CrossRef](#)] [[PubMed](#)]
43. Kawashima, H.; Hirose, M.; Hirose, J.; Nagakubo, D.; Plaas, A.H.; Miyasaka, M. Binding of a large chondroitin sulfate/dermatan sulfate proteoglycan, versican, to L-selectin, P-selectin, and CD44. *J. Biol. Chem.* **2000**, *275*, 35448–35456. [[CrossRef](#)] [[PubMed](#)]
44. Zheng, P.-S.; Vais, D.; Lapierre, D.; Liang, Y.-Y.; Lee, V.; Yang, B.L.; Yang, B.B. PG-M/versican binds to P-selectin glycoprotein ligand-1 and mediates leukocyte aggregation. *J. Cell Sci.* **2004**, *117*, 5887–5895. [[CrossRef](#)]
45. Wu, Y.J.; Pierre, D.P.L.A.; Wu, J.; Yee, A.J.; Yang, B.B. The interaction of versican with its binding partners. *Cell Res.* **2005**, *15*, 483–494. [[CrossRef](#)]
46. Hirano, Y.; Sakurai, E.; Matsubara, A.; Ogura, Y. Suppression of ICAM-1 in Retinal and Choroidal Endothelial Cells by Plasmid Small-Interfering RNAs In Vivo. *Investig. Ophthalmol. Vis. Sci.* **2010**, *51*, 508–515. [[CrossRef](#)]
47. Granot, E.; Shouval, D.; Ashur, Y. Cell adhesion molecules and hyaluronic acid as markers of inflammation, fibrosis and response to antiviral therapy in chronic hepatitis C patients. *Mediat. Inflamm.* **2001**, *10*, 274192. [[CrossRef](#)] [[PubMed](#)]

48. Yang, X.; Chung, J.-Y.; Rai, U.; Esumi, N. Cadherins in the retinal pigment epithelium (RPE) revisited: P-cadherin is the highly dominant cadherin expressed in human and mouse RPE in vivo. *PLoS ONE* **2018**, *13*, e0191279. [[CrossRef](#)]
49. Poliseti, N.; Sharaf, L.; Martin, G.; Schlunck, G.; Reinhard, T. P-Cadherin Is Expressed by Epithelial Progenitor Cells and Melanocytes in the Human Corneal Limbus. *Cells* **2022**, *11*, 1975. [[CrossRef](#)]
50. Aimo, A.; Spitaleri, G.; Nieri, D.; Tavanti, L.M.; Meschi, C.; Panichella, G.; Lupón, J.; Pistelli, F.; Carrozzi, L.; Bayes-Genis, A.; et al. Pirfenidone for Idiopathic Pulmonary Fibrosis and Beyond. *Card. Fail. Rev.* **2022**, *8*, e12. [[CrossRef](#)]
51. Adler, M.; Mayo, A.; Zhou, X.; Franklin, R.A.; Meizlish, M.L.; Medzhitov, R.; Kallenberger, S.M.; Alon, A. Principles of Cell Circuits for Tissue Repair and Fibrosis. *iScience* **2020**, *23*, 100841. [[CrossRef](#)] [[PubMed](#)]
52. Jun, J.I.; Lau, L.F. Resolution of organ fibrosis. *J. Clin. Investig.* **2018**, *128*, 97–107. [[CrossRef](#)]
53. Rodrigues, R.M.; He, Y.; Hwang, S.; Bertola, A.; Mackowiak, B.; Ahmed, Y.A.; Seo, W.; Ma, J.; Wang, X.; Park, S.H.; et al. E-Selectin-Dependent Inflammation and Lipolysis in Adipose Tissue Exacerbate Steatosis-to-NASH Progression via S100A8/9. *Cell Mol. Gastroenterol. Hepatol.* **2022**, *13*, 151–171. [[CrossRef](#)] [[PubMed](#)]
54. Zhang, N.; Liu, Z.; Yao, L.; Mehta-D'souza, P.; McEver, R.P. P-Selectin Expressed by a Human SELP Transgene Is Atherogenic in Apolipoprotein E-Deficient Mice. *Arterioscler. Thromb. Vasc. Biol.* **2016**, *36*, 1114–1121. [[CrossRef](#)] [[PubMed](#)]
55. Corona, A.; Blobe, G.C. The role of the extracellular matrix protein TGFBI in cancer. *Cell Signal.* **2021**, *84*, 110028. [[CrossRef](#)]
56. Cabral-Pacheco, G.A.; Garza-Veloz, I.; Castruita-De la Rosa, C.; Ramirez-Acuña, J.M.; Perez-Romero, B.A.; Guerrero-Rodriguez, J.F.; Martinez-Avila, N.; Martinez-Fierro, M.L. The Roles of Matrix Metalloproteinases and Their Inhibitors in Human Diseases. *Int. J. Mol. Sci.* **2020**, *21*, 9739. [[CrossRef](#)]
57. Jahnke, L.; Zandi, S.; Elhelbawi, A.; Conedera, F.M.; Enzmann, V. Characterization of Macrogia Response during Tissue Repair in a Laser-Induced Model of Retinal Degeneration. *Int. J. Mol. Sci.* **2023**, *24*, 9172. [[CrossRef](#)]

Disclaimer/Publisher's Note: The statements, opinions and data contained in all publications are solely those of the individual author(s) and contributor(s) and not of MDPI and/or the editor(s). MDPI and/or the editor(s) disclaim responsibility for any injury to people or property resulting from any ideas, methods, instructions or products referred to in the content.